Polyhedral Bimetallic Alloy Nanocrystals Exclusively Bound by {110} Facets: Au–Pd Rhombic Dodecahedra**

Young Wook Lee, Minjung Kim, Shin Wook Kang, and Sang Woo Han*

Controlled synthesis of nanocrystals (NCs) with well-defined morphologies is an important subject in the field of nano-technology because intrinsic physicochemical properties of nanostructures strongly depend on their shapes.[1] In particular, fine-tuning of the optical and electronic characteristics of noble metal NCs by tailoring their morphologies has been extensively studied because of their promising applications in plasmonics, nanoelectronics, and surface-enhanced Raman scattering (SERS)-based diagnosis.[2–4] Furthermore, the shape of metal NCs has a profound influence on their catalytic activity and selectivity in a variety of chemical reactions.[5–10] This observation can be attributed to the different types of exposed crystallographic planes (facets) on their surfaces, which can determine the overall catalytic properties of the NCs.

Although a number of shaped NCs have been synthesized over the past decade, most NCs of noble metals with face-centered cubic (fcc) structure are bound by low-index {111} and {100} surfaces owing to minimization of surface energy during NC growth.[11] Recently, we and others have succeeded in preparing noble metal NCs enclosed completely by {110} facets, which have the highest surface energy among the low-index facets, such as Au and Pd rhombic dodecahedra.[12–16] There are also a few reports on production of metal NCs with exposed high-index {hk0} and {hhl} (h > 1) facets.[17–22] However, compared to monometallic NCs, engineering crystalline facets by shape-controlled synthesis of bimetallic alloy NCs has been limited due to the complex reduction kinetics of metal precursors and the difficulty in finding suitable structure-directing agents. In particular, alloy NCs bound by high-energy facets have been little explored to date. Here we report on the synthesis of rhombic dodecahedral (RD) Au–Pd bimetallic alloy NCs enclosed exclusively by 12 {110} facets in high yield by a simple one-pot aqueous synthetic method. Since bimetallic NCs often exhibit better physical and

chemical properties than their monometallic counterparts and these properties can be modulated by controlling the shape and exposed facets of the NCs,[9,23–27] development of efficient synthetic strategies for alloy NCs with desirable structures is important.

One-pot synthesis of RD Au–Pd NCs was achieved by co-reduction of Au and Pd precursors with ascorbic acid in the presence of cetyltrimethylammonium chloride (CTAC). In a typical synthesis, aqueous solutions of an equimolar $HAuCl_4$/K_2PdCl_4 mixture, ascorbic acid, and CTAC were mixed, and the resultant solution was kept under ambient conditions for about 1 h. A representative SEM image of the asprepared product (Figure 1a) shows that the majority of the sample
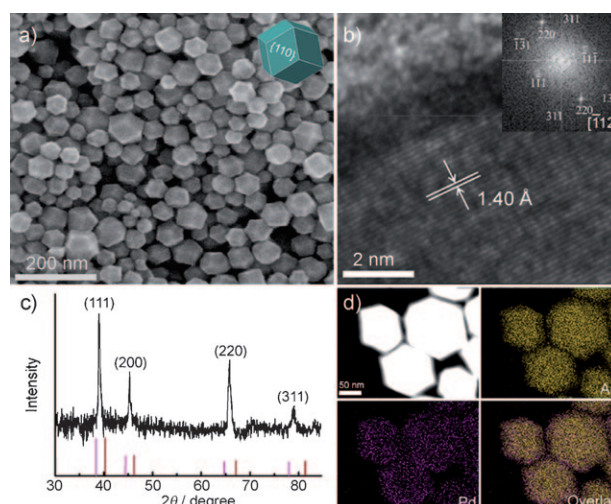

Figure 1. a) SEM image of RD Au–Pd NCs. The inset shows an ideal RD structure bound by 12 {110} surfaces. b) High-magnification HRTEM image of an RD Au–Pd NC. The corresponding selected-area FFT pattern is shown in the inset. c) XRD pattern of RD Au–Pd NCs. The intensities and positions for pure Au (pink lines at the bottom) and Pd (brown lines at the bottom) references were taken from the JCPDS database. d) HAADF-STEM-EDS mapping images of the RD Au–Pd NCs.

(>85%) consists of RD NCs with an average edge length of 48 ± 7 nm. An ideal RD structure bound by 12 {110} surfaces (inset of Figure 1a) matches well with the synthesized NCs. The prepared NCs were stable in aqueous solution for up to several weeks under ambient conditions. The HRTEM image demonstrates that the exposed surfaces of the NCs are bound by {110} facets; the *d* spacing of 1.40 Å for adjacent lattice fringes corresponds to that of the (220) plane of fcc Au–Pd (Figure 1b). The selected area fast Fourier transform (FFT) pattern displayed in the inset of Figure 1b also shows that the

[*] Y. W. Lee, M. Kim, S. W. Kang, Prof. S. W. Han
Department of Chemistry and KI for the NanoCentury
KAIST, Daejeon 305-701 (Korea)
Fax: (+82) 42-350-2810
E-mail: sangwoohan@kaist.ac.kr
Homepage: http://ntl.kaist.ac.kr

prepared NC is a single crystal. Figure 1c shows the XRD pattern of the RD Au–Pd NCs. The characteristic diffraction peaks of the fcc structure of metallic Au–Pd can be observed, and peak positions intermediate between those of pure Au and Pd reveal the formation of single-phase Au–Pd alloy. Elemental mapping of Au and Pd (Figure 1d) and the compositional line profiles on a single NC (Figure S1 in the Supporting Information) obtained by high-angle annular dark-field scanning TEM and energy-dispersive X-ray spectroscopy (HAADF-STEM-EDS) reveal that the prepared NCs are definitely Au–Pd alloy. The Au/Pd atomic ratio of the RD Au–Pd NCs was estimated to be 78/22 by inductively coupled plasma atomic emission spectrometry (ICP-AES). The higher Au/Pd ratio than in the raw solution may be attributable to the higher reduction potential of $AuCl_4^-$ [$AuCl_4^-$/Au: +1.002 V vs. standard hydrogen electrode (SHE)] compared to $PdCl_4^{2-}$ ($PdCl_4^{2-}$/Pd: +0.591 V vs. SHE).[28]

The formation process of the NCs could be monitored by TEM measurements at different reaction times (Figure 2). Initially, small NCs grew within about 5 min (Figure 2a).
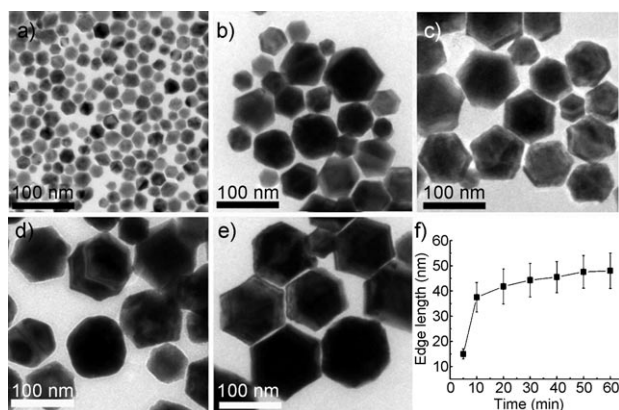

Figure 2. TEM images of NCs collected at different reaction times. a) 5, b) 20, c) 30, d) 40, and e) 60 min. f) Change in the edge length of NCs during the reaction, estimated by TEM analysis.

Close inspection of the TEM images of the initially formed NCs clearly shows that most of the NCs have RD shape with a mean edge length of 15 ± 2 nm (Figure 3a and b). Elemental mapping (Figure 3c) and the compositional line profiles (Figure 3d) obtained by HAADF-STEM-EDS also revealed the alloy nature of the NCs. As the reaction proceeded, the NCs grew in size over about 1 h (Figure 2b–f). Beyond 1 h, no significant change in structure was observed. These findings imply that the Au–Pd alloy NCs with RD morphology evolved at the very early stages of the reaction and then acted as seeds for further NC growth. Changes in the size of the NCs during the reaction further indicate that NC size can be controlled by means of different reaction times. The NC size could also be modulated by varying the amount of CTAC. For example, a twofold increase in the amount of CTAC under otherwise identical synthetic conditions gave RD Au–Pd NCs with an edge length of 75 nm (Figure S2 in the Supporting Information), which may be ascribed to the fact that the larger amount
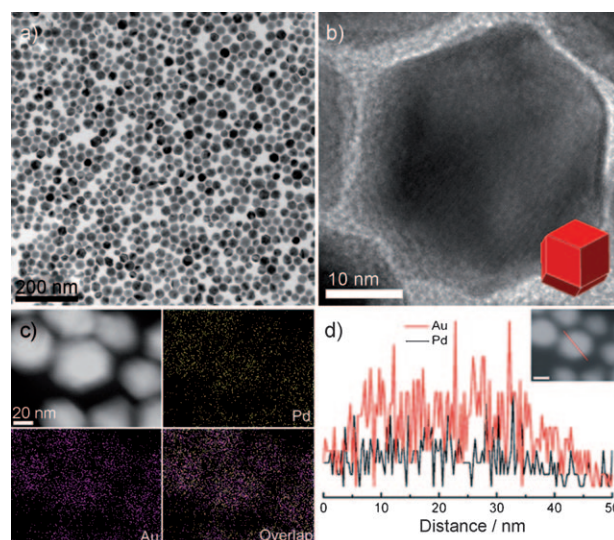

Figure 3. a) TEM and b) HRTEM images of the Au–Pd NCs after a reaction time of 5 min. The inset in b) shows the three-dimensional structural model of an ideal rhombic dodecahedron. c) HAADF-STEM-EDS mapping images of the Au–Pd NCs. d) HAADF-STEM image and cross-sectional compositional line profiles of an Au–Pd NC. Scale bar: 20 nm.

of surfactant releases fewer Au and Pd atoms for nucleation and thus decreases the number of seeds and results in formation of larger NCs.[29]

Formation of RD Au–Pd NCs may result from a kinetically controlled nucleation and growth process. Recently, we found that Au@Pd core–shell NCs with {111}-faceted octahedral structure were formed when $AuCl_4^-$ and $PdCl_4^{2-}$ precursors were co-reduced by CTAC in the absence of ascorbic acid.[30] Due to the weak reducing power of CTAC, it took about 48 h to complete the reaction even at elevated temperature (ca. 90°C). This slow reduction kinetics facilitated thermodynamic control over nucleation/growth of the NCs; formation of the Au@Pd NCs was initiated by nucleation of Au atoms to form an Au octahedral core bound by thermodynamically stable {111} facets, followed by the epitaxial growth of a Pd layer onto the Au core. On the basis of this finding, we believe that the RD Au–Pd NCs enclosed by the high-energy {110} facets are kinetically trapped under our experimental conditions. On the other hand, cationic surfactant CTAC as capping agent plays a critical role in formation of the RD Au–Pd NCs with exposed high-energy {110} surfaces. Reportedly, CTAC can drive the formation of metal NCs enclosed by high-energy facets through preferential adsorption of CTA$^+$ on these facets rather than on low-energy ones.[18,21] In fact, we could not obtain RD NCs when CTAC was replaced by other commonly used capping agents such as polyvinylpyrrolidone (PVP), cetyltrimethylammonium bromide (CTAB), sodium dodecyl sulfate (SDS), and tetraoctylammonium bromide (TOAB), as shown in Figure S3 of the Supporting Information. Recently, we reported that simultaneous reduction of $HAuCl_4$ and K_2PdCl_4 by ascorbic acid in the presence of PVP yields popcorn-shaped Au–Pd alloy nanoparticles (NPs) enclosed predominantly by {111} facets.[31] The production of irregular

particles on using CTAB, which has the same cation as CTAC, suggests that the Cl⁻ counteranion is also important in formation of NCs. The Br⁻ ion has a strong binding affinity to metal surfaces, and thus alters the binding scheme of CTA⁺ onto the NC surface and the relative growth rates between different facets.[13,18,21]

Control experiments with different molar ratios of $HAuCl_4$ and K_2PdCl_4 also revealed that the Au/Pd ratio in the precursor solution is a key to formation of RD NCs. The NCs synthesized by using only $HAuCl_4$ as metal precursor have truncated octahedral and decahedral shapes, while irregularly shaped Pd NPs were produced under identical conditions in the absence of $HAuCl_4$ (Figure S4 in the Supporting Information). Thus, both Au and Pd precursors are necessary for growth of RD NCs. In addition, reactions with 3/1 and 1/3 molar ratios of $HAuCl_4/K_2PdCl_4$ did not lead to formation of RD NCs; instead, roughly truncated octahedral NCs were produced (Figure S5 in the Supporting Information), which are enclosed dominantly by {111} facets (Figure S6 in the Supporting Information). These results demonstrate that the metal precursors, $HAuCl_4$ and K_2PdCl_4, also play a vital role in the control of NC structure. This may be due to modulation of the reduction kinetics through variation of the relative amounts of each metal precursor; synthesis of RD Au–Pd NCs could be achieved when an appropriate $HAuCl_4/K_2PdCl_4$ molar ratio was used. Similar observations have also been reported. For instance, monodisperse Au–Cu bimetallic nanocubes were prepared by using Cu(acetylacetonate)$_2$ and $HAuCl_4$ as both metal precursors and effective structure-directing agents.[32]

The exposed {110} surfaces of the synthesized NCs might be expected to benefit a number of applications, such as the development of efficient SERS platforms with unprecedented activities, because high-energy {110} surfaces are believed to have higher SERS activity than the other low-index facets {111} and {100}.[12,33] To investigate the SERS activity of the RD Au–Pd NCs, we measured SERS spectra of various analytes such as 1,4-phenylene diisocyanide (1,4-PDI), 4-aminobenzenethiol (4-ABT), benzenethiol (BT), and rhodamine 6G (R6G) adsorbed on the NCs, and compared them with those obtained on predominantly {111} faceted popcornlike Au–Pd alloy NPs with similar composition (Au/Pd atomic ratio 69/31, Figure S7 in the Supporting Information). The two substrates exhibited similar surface plasmon features in the UV/Vis extinction spectra (Figure S8 in the Supporting Information). The RD Au–Pd NCs give stronger SERS signals than the Au–Pd NPs for all adsorbates tested (Figure 4); the SERS intensities obtained with the RD NCs are at least two times higher than those with the Au–Pd NPs. Since the SERS intensity depends on the packing density of the nanostructures on the surface, all SERS spectra shown in Figure 4 were obtained by averaging more than ten spectra recorded at different areas on the surface. Although the exact origin of the enhanced SERS activity of the RD NCs is not clear at present, it can be assumed that the {110} facets of the NCs endow them with high SERS activity. However, the stronger SERS signals from the RD NCs compared to the NPs may also be ascribed to the presence of sharp edges and apexes on the surface of the RD NCs, which could serve as "hot spots"
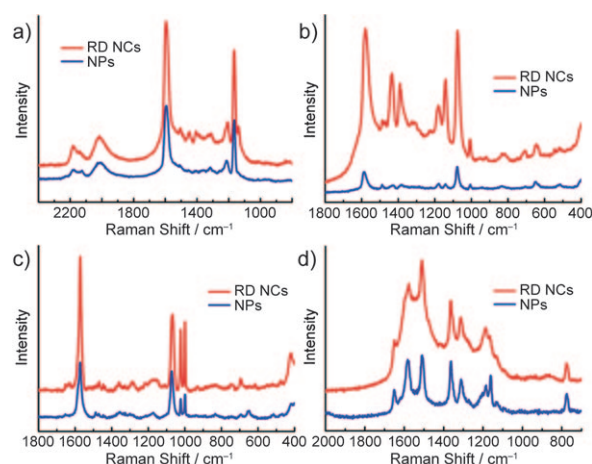

Figure 4. SERS spectra of a) 1,4-PDI, b) 4-ABT, c) BT, and d) R6G on RD Au–Pd NCs and popcornlike Au–Pd alloy NPs.

for SERS.[34,35] Detailed studies on the facet-dependent SERS activity are currently underway.

The electrocatalytic activity of noble metal NCs has been intensively studied on different exposed surfaces. To investigate the influence of surface facets on the catalytic performance of NCs, the electrocatalytic properties of the RD Au–Pd NCs in ethanol oxidation were examined and compared with those of the predominantly {111} faceted Au–Pd alloy NPs. Pd-based nanostructures are known to be efficient electrocatalysts for ethanol oxidation in alkaline media, and incorporation of Au into Pd catalysts further improves catalytic activity and selectivity as well as resistance to poisoning.[36] Figure 5a shows the cyclic voltammograms (CVs) of a glassy carbon electrode (GCE) modified with the RD Au–Pd NCs and Au–Pd NPs in 0.1 M KOH. Typical redox peaks associated with the oxidation/reduction of Au–Pd alloy are observed.[37] The current densities were normalized to the electrochemically active surface areas (ECSA).[38] The obser-
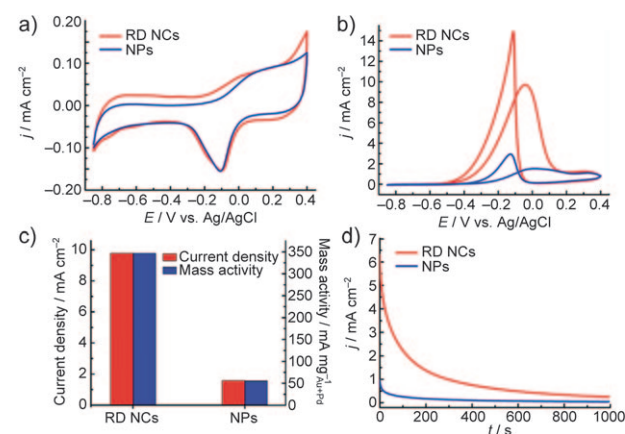

Figure 5. CVs of RD Au–Pd NCs and the popcornlike Au–Pd alloy NPs on GCE in a) 0.1 M KOH and b) 0.1 M KOH + 0.5 M ethanol. Scan rate: 50 mVs⁻¹. Currents were normalized with respect to the ECSA. c) Current densities and mass activities for ethanol oxidation on the RD NCs and NPs. d) CA curves of RD NCs and NPs on GCE in 0.1 M KOH + 0.5 M ethanol at −0.1 V vs. Ag/AgCl.

vation of single reduction peak for each sample with the same potential of about −0.1 V versus Ag/AgCl demonstrates that Au and Pd atoms are homogeneously distributed on the surfaces of the Au–Pd RD NCs and NPs, and the surface compositions of the two samples are very similar.[37,39] Figure 5b displays the ethanol electrooxidation activities on different catalysts in 0.1 M KOH solution containing 0.5 M ethanol. Characteristic well-separated anodic peaks in the forward and reverse potential scans associated with ethanol oxidation are observed. Notably, the onset potential of the RD Au–Pd NCs is more negative than that of the Au–Pd NPs (−0.50 and −0.35 V vs. Ag/AgCl, respectively). In addition, the ECSA-normalized current density of the RD Au–Pd NCs is much higher than that of the Au–Pd alloy NPs. In the forward scan, the peak current density of the RD Au–Pd NCs is 9.78 mA cm^{-2}, which is about 6.2 times higher than that of the Au–Pd NPs (1.58 mA cm^{-2}; Figure 5c). Moreover, the corresponding mass activity of the RD Au–Pd NCs is 346.8 mA mg$_{Au+Pd}^{-1}$, whereas that of the Au–Pd NPs is 55.3 mA mg$_{Au+Pd}^{-1}$ (Figure 5c and Figure S9 in the Supporting Information). These findings clearly indicate that the RD Au–Pd NCs have markedly enhanced electrocatalytic activity for ethanol oxidation compared to the Au–Pd NPs. Chronoamperometry (CA) experiments at −0.1 V versus Ag/AgCl also reveal that the electrochemical stability of the RD Au–Pd NCs in ethanol electro-oxidation is superior to that of the Au–Pd NPs (Figure 5d). The enhanced electrocatalytic activity and stability of the RD Au–Pd NCs may be attributed to their exposed highly reactive {110} surfaces, which originate from their dodecahedral structure.

In summary, we have developed a facile one-pot synthesis of RD Au–Pd alloy NCs bound entirely by {110} facets. Formation of this unique structure was achieved through a kinetically controlled nucleation and growth process. The RD NCs exhibit higher SERS and electrocatalytic activities than {111}-faceted NPs. We expect that the exposed high-energy {110} surfaces of the NCs will promote their potential optical and catalytic applications, and the present work may be extendable to fabrication of other multicomponent metal NCs with desirable morphologies.

Experimental Section

HAuCl$_4$ (Aldrich, 99.99 + %), K$_2$PdCl$_4$ (Aldrich, 98%), ascorbic acid (Dae Jung Chemicals & Metals Co., 99.5%), CTAC (Aldrich, solution in water, 25 wt%), sodium citrate dihydrate (Aldrich, 99%), CTAB (Aldrich, 95%), SDS (Fluka, 99%), TOAB (Aldrich, 98%), and PVP (M_W = 55 000) were used as received. Other chemicals, unless specified, were of reagent grade, and Milli-Q water with a resistivity greater than 18.0 MΩ cm was used in the preparation of aqueous solutions.

In a typical synthesis of RD Au–Pd NCs, 1 mL of a 5 mM aqueous solution of HAuCl$_4$/K$_2$PdCl$_4$ (molar ratio 1/1) was added to an aqueous solution of CTAC (5 mL, 50 mM), and then an aqueous solution of ascorbic acid (100 mM, 50 μL) was added to this mixture. The resultant reaction solution was kept under ambient conditions for about 1 h. The resultant hydrosol was subjected to centrifugation (6000 rpm for 5 min, twice) to remove excess reagent.

The extinction spectra were recorded with a UV/Vis absorption spectrometer (Agilent 8453). SEM images of the samples were taken with a field-emission scanning electron microscope (FESEM, Phillips

Model XL30 S FEG). TEM images were obtained with a Phillips Model Tecnai F20 transmission electron microscope operating at 200 kV after placing a drop of hydrosol on carbon-coated Cu grids (200 mesh). HRTEM and HAADF-STEM characterizations were performed with a FEI Tecnai G2 F30 Super-Twin transmission electron microscope operating at 300 kV. The effective electron probe size and dwell time used in HAADF-STEM-EDS mapping experiments were 1.5 nm and 200 ms per pixel, respectively. The compositions of the NCs were determined by ICP-AES (OPTIMA 3300DV). XRD patterns were obtained on a Bruker AXS D8 DISCOVER diffractometer with Cu$_{Kα}$ (0.1542 nm) radiation. For Raman measurement, drop-cast films of NCs on Si substrates were soaked overnight in analyte solution in ethanol (10^{-4} M for 1,4-PDI, 4-ABT, and BT; 10^{-6} M for R6G). The substrate was removed from the solution, washed thoroughly with ethanol, and dried under ambient conditions. Raman spectra were obtained on a Jobin Yvon/HORIBA LabRAM spectrometer equipped with an integral microscope (Olympus BX 41). The 632.8 nm line of an air-cooled He/Ne laser was used as excitation source. Raman scattering was detected with 180° geometry by using a thermoelectrically cooled 1024 × 256-pixel charge coupled device (CCD) detector. The laser beam (1.5 mW) was focused onto a spot (ca. 1 μm diameter) with an objective lens (× 50, NA = 0.50). Data acquisition times were usually 60 s. The holographic grating (1800 grooves/mm) and the slit allowed a spectral resolution of 1 cm^{-1}. The Raman band of an Si wafer at 520 cm^{-1} was used to calibrate the spectrometer. Cyclic voltammetry (CV) measurements were carried out in a three-electrode cell by using a CH Instrument Model 600C potentiostat. Drop-cast films of NCs on GCE (diameter: 3 mm) served as working electrodes. Before CV measurements, 4 μL of aqueous NC solution (0.5 μg$_{Au+Pd}$ μL^{-1} according to ICP-AES), which was obtained by centrifugation, was dropped onto a GCE (metal loading: 28 μg cm^{-2}). After the solution was dried, 4 μL of Nafion solution (0.05%) was added, and then dried in a Dry-Keeper. The dried working electrode was cleaned by sequentially washing with ethanol and water, and then electrochemically cleaned by 50 potential cycles between −0.8 and 0.4 V at a scan rate of 50 mV s^{-1} to remove residual stabilizing agents on the surface of the NCs. Pt wire and Ag/AgCl (in saturated KCl) were used as the counter- and reference electrodes, respectively. All CVs were obtained at room temperature, and the electrolyte solutions were purged with high-purity N$_2$ gas for about 1 h before use.

[1] C. Burda, X. Chen, R. Narayanan, M. A. El-Sayed, *Chem. Rev.* **2005**, *105*, 1025.
[2] N. L. Rosi, C. A. Mirkin, *Chem. Rev.* **2005**, *105*, 1547.
[3] A. R. Tao, S. E. Habas, P. Yang, *Small* **2008**, *4*, 310.
[4] Y. Xia, Y. Xiong, B. Lim, S. E. Skrabalak, *Angew. Chem.* **2009**, *121*, 62; *Angew. Chem. Int. Ed.* **2009**, *48*, 60.
[5] R. Narayanan, M. A. El-Sayed, *Nano Lett.* **2004**, *4*, 1343.
[6] S. E. Habas, H. Lee, V. Radmilovic, G. A. Somorjai, P. Yang, *Nat. Mater.* **2007**, *6*, 692.
[7] C. Wang, H. Daimon, T. Onodera, T. Koda, S. Sun, *Angew. Chem.* **2008**, *120*, 3644; *Angew. Chem. Int. Ed.* **2008**, *47*, 3588.
[8] Z. Peng, H. Yang, *Nano Today* **2009**, *4*, 143.
[9] S.-I. Choi, R. Choi, S. W. Han, J. T. Park, *Chem. Commun.* **2010**, *46*, 4950.
[10] Y. W. Lee, M. Kim, S. W. Han, *Chem. Commun.* **2010**, *46*, 1535.
[11] Y. Xiong, B. J. Wiley, Y. Xia, *Angew. Chem.* **2007**, *119*, 7291; *Angew. Chem. Int. Ed.* **2007**, *46*, 7157.

[12] G. H. Jeong, M. Kim, Y. W. Lee, W. Choi, W. T. Oh, Q.-H. Park, S. W. Han, *J. Am. Chem. Soc.* **2009**, *131*, 1672.

[13] W. Niu, S. Zheng, D. Wang, X. Liu, H. Li, S. Han, J. Chen, Z. Tang, G. Xu, *J. Am. Chem. Soc.* **2009**, *131*, 697.

[14] D. Y. Kim, S. H. Im, O. O. Park, Y. T. Lim, *CrystEngComm* **2010**, *12*, 116.

[15] W. Niu, L. Zhang, G. Xu, *ACS Nano* **2010**, *4*, 1987.

[16] C.-L. Lu, K. S. Prasad, H.-L. Wu, J. A. Ho, M. H. Huang, *J. Am. Chem. Soc.* **2010**, *132*, 14546.

[17] N. Tian, Z. Zhou, S. Sun, Y. Ding, Z. L. Wang, *Science* **2007**, *316*, 732.

[18] Y. Ma, Q. Kuang, Z. Jiang, Z. Xie, R. Huang, L. Zheng, *Angew. Chem.* **2008**, *120*, 9033; *Angew. Chem. Int. Ed.* **2008**, *47*, 8901.

[19] H.-G. Liao, Y.-X. Jiang, Z.-Y. Zhou, S.-P. Chen, S.-G. Sun, *Angew. Chem.* **2008**, *120*, 9240; *Angew. Chem. Int. Ed.* **2008**, *47*, 9100.

[20] T. Ming, W. Feng, Q. Tang, F. Wang, L. Sun, J. Wang, C. Yan, *J. Am. Chem. Soc.* **2009**, *131*, 16350.

[21] Y. Yu, Q. Zhang, X. Lu, J. Y. Lee, *J. Phys. Chem. C* **2010**, *114*, 11119.

[22] J. Zhang, M. R. Langille, M. L. Personick, K. Zhang, S. Li, C. A. Mirkin, *J. Am. Chem. Soc.* **2010**, *132*, 14012.

[23] R. Ferrando, J. Jellineck, R. L. Johnston, *Chem. Rev.* **2008**, *108*, 845.

[24] D. Xu, Z. Liu, H. Yang, Q. Liu, J. Zhang, J. Fang, S. Zou, K. Sun, *Angew. Chem.* **2009**, *121*, 4281; *Angew. Chem. Int. Ed.* **2009**, *48*, 4217.

[25] Y. Kang, C. B. Murray, *J. Am. Chem. Soc.* **2010**, *132*, 7568.

[26] J. Wu, J. Zhang, Z. Peng, S. Yang, F. T. Wagner, H. Yang, *J. Am. Chem. Soc.* **2010**, *132*, 4984.

[27] J. Zhang, H. Yang, J. Fang, S. Zou, *Nano Lett.* **2010**, *10*, 638.

[28] K. Y. Lee, M. Kim, Y. W. Lee, J.-J. Lee, S. W. Han, *Chem. Phys. Lett.* **2007**, *440*, 249.

[29] S. Saita, S. Maenosono, *Chem. Mater.* **2005**, *17*, 6624.

[30] Y. W. Lee, M. Kim, Z. H. Kim, S. W. Han, *J. Am. Chem. Soc.* **2009**, *131*, 17036.

[31] Y. W. Lee, N. H. Kim, K. Y. Lee, K. Kwon, M. Kim, S. W. Han, *J. Phys. Chem. C* **2008**, *112*, 6717.

[32] Y. Liu, A. R. H. Walker, *Angew. Chem.* **2010**, *122*, 6933; *Angew. Chem. Int. Ed.* **2010**, *49*, 6781.

[33] J. Zhang, X. Li, X. Sun, Y. Li, *J. Phys. Chem. B* **2005**, *109*, 12544.

[34] K. Kneipp, H. Kneipp, J. Kneipp, *Acc. Chem. Res.* **2006**, *39*, 443.

[35] J. Heo, D.-S. Kim, Z. H. Kim, Y. W. Lee, D. Kim, M. Kim, K. Kwon, H. J. Park, W. S. Yun, S. W. Han, *Chem. Commun.* **2008**, 6120.

[36] C. Bianchini, P. K. Shen, *Chem. Rev.* **2009**, *109*, 4183.

[37] R. Woods in *Electroanalytical Chemistry: A Series of Advances*, *Vol. 9* (Ed.: A. J. Bard), Marcel Dekker, New York, **1974**, pp. 1–162.

[38] The ECSA was estimated as $ECSA = Q_o/q_o$, where Q_o is the surface charge obtained from the area under the CV trace for reduction of metal oxide, and q_o the charge required for desorption of monolayer of oxygen on the Au–Pd surface (406 $\mu C\,cm^{-2}$).[37]

[39] M. Tominaga, T. Shimazoe, M. Nagashima, H. Kusuda, A. Kubo, Y. Kuwahara, I. Taniguchi, *J. Electroanal. Chem.* **2006**, *590*, 37.